Journal of the Optical Society of America B
OPTICAL PHYSICS

Focused-beam optical potentials for cold atoms near an atom chip

ALAN ZANDERS[1,*] AND SHENGWANG DU[1,2,3,4]

[1]Department of Physics, University of Texas at Dallas, Richardson, Texas 75080, USA
[2]Elmore Family School of Electrical and Computer Engineering, Purdue University, West Lafayette, Indiana 47907, USA
[3]Department of Physics and Astronomy, Purdue University, West Lafayette, Indiana 47907, USA
[4]Purdue Quantum Science and Engineering Institute, Purdue University, West Lafayette, Indiana 47907, USA
*Alan.Zanders@utdallas.edu

Received 18 February 2026; revised 28 April 2026; accepted 23 June 2026; posted 24 June 2026; published 11 August 2026

Precise alignment of an optical potential with a micrometer-scale magnetic trap near an atom chip is technically challenging compared with free-space systems. We investigate a double-well potential created by a focused, blue-detuned laser beam superimposed on an atom-chip magnetic trap for manipulating cold ^{87}Rb atoms. The measured separation of atomic clouds in the double well serves as a sensitive indicator of the laser focus: the separation reaches a minimum when the beam is aligned with the center of the magnetic trap. We develop a theoretical model for the combined magnetic and optical potentials and the resulting atomic motion, and validate its predictions using Monte Carlo simulations over a broad range of trap frequencies, barrier heights, and temperatures. Both the model and simulations show that optimal alignment corresponds to the minimum observable separation between the two atomic clouds. Parameter scans further reveal that stronger axial confinement and lower temperatures enhance the detectability of this minimum, providing a practical optical-alignment method for atom-chip systems in which direct beam characterization near the surface is difficult.

https://doi.org/10.1364/JOSAB.595759

1. INTRODUCTION

Cold atomic ensembles confined in magnetic and optical potentials provide a versatile platform for studying classical dynamics [1,2], thermally driven transport [3], and the emergence of quantum behavior [4–6]. Among these configurations, double-well potentials are particularly valuable for exploring symmetry breaking, equilibration, and tunneling phenomena [7,8]. They serve as benchmark systems for investigating nonequilibrium dynamics and coherent control in ultracold gases.

In atom-chip experiments, magnetic confinement is typically generated by current-carrying microstructures that form a three-dimensional harmonic potential [9,10]. When a blue-detuned Gaussian laser beam is aligned along the short axis of the trap, it introduces a localized repulsive barrier that divides the magnetic trap into two wells. The resulting double-well geometry is highly sensitive to the optical beam's alignment and focal position: even sub-micrometer offsets can create asymmetries in the potential landscape, leading to unbalanced atomic populations and distorted trap profiles that compromise reproducibility and tunneling measurements [11].

Although double-well configurations are widely employed in cold-atom research [12–15], systematic studies of how optical-beam alignment and focus affect atom-chip traps remain scarce. Alignment is often treated as a technical step, yet it has a direct influence on the potential geometry and, consequently, on the interpretation of experimental observables. This sensitivity is especially pronounced in the cold, predominantly classical regime, where quantum tunneling is weak and the atomic distributions primarily reflect the underlying potential landscape.

Here, we address this gap by presenting a simulation-based investigation of cold ^{87}Rb atoms confined in a magnetic trap bisected by a repulsive optical barrier. We show that the measured separation between the two atomic clouds provides a sensitive indicator of the laser focus: the separation reaches a minimum when the beam is centered within the magnetic trap. Monte Carlo simulations over a wide range of temperatures (1 μK−10 mK) and axial trap frequencies (100 Hz−10 kHz) confirm this relationship, while variations in the transverse confinement have negligible effect. The results establish a practical method for optimizing optical alignment in hybrid atom-chip systems, where direct beam characterization near the chip surface is challenging.

2. THEORY AND MODEL

In atom-chip experiments, magnetic confinement is generated by microfabricated current-carrying traces that produce

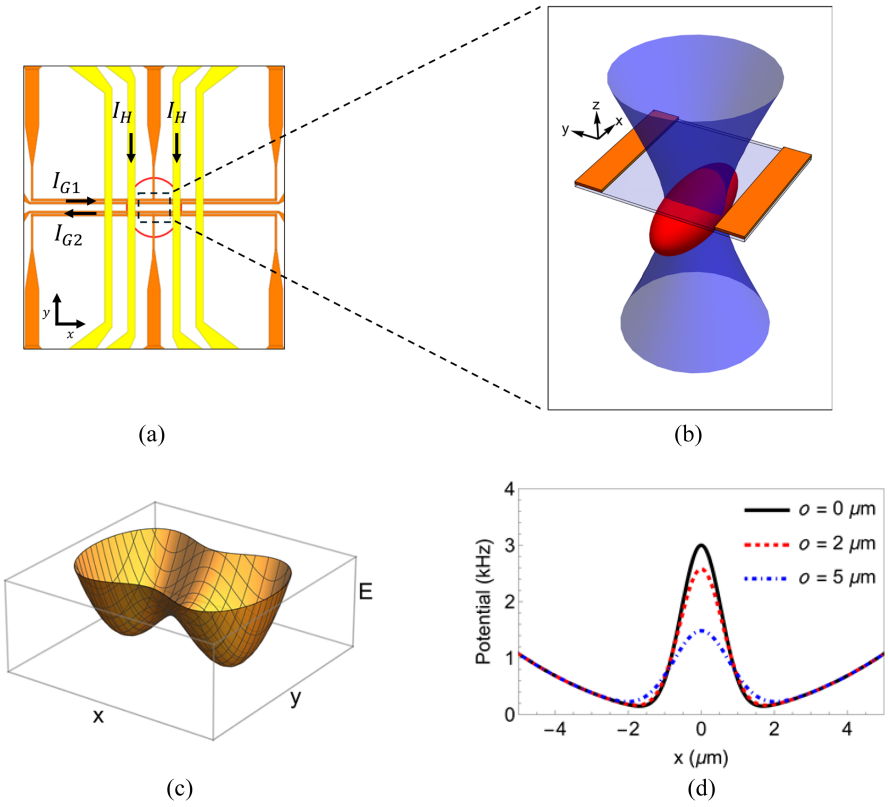

Fig. 1. General setup: (a) atom-chip traces generating the magnetic trap, (b) overlap of the trapped atomic cloud (red) with the Gaussian optical barrier (blue), (c) typical combined potential from the atom-chip trap and the Gaussian barrier, and (d) axial potential cross-sections for a 3 kHz barrier at different axial offsets o.

a three-dimensional harmonic potential, as shown in Fig. 1(a) with currents I_{G1}, I_{G2}, and I_H. A blue-detuned Gaussian beam introduces a repulsive barrier along the z axis, forming a double-well potential whose symmetry and effective depth depend sensitively on the axial alignment and focal position of the beam, as shown in Figs. 1(b) and 1(c). Even a small axial offset between the magnetic trap center and the optical waist minimum can significantly modify the barrier height and width [Fig. 1(d)], and hence the observed cloud separation.

At focus, the beam waist is minimized, and the barrier is narrowest and highest. Away from focus, the waist increases according to Gaussian-beam propagation, decreasing the peak intensity and broadening the barrier. Although one might initially expect that the optimal alignment depends on temperature—e.g., low-T atoms being sensitive primarily to width and high-T atoms to height—our simulations and analytical modeling show that across the experimentally relevant temperature range and axial trap frequencies, the correct optimization criterion is always to minimize the measured cloud separation.

A. Magnetic and Optical Potentials

We model the atom-chip magnetic confinement as a harmonic trap,

$$U_B(x, y, z) = \frac{1}{2} m \left(\omega_x^2 x^2 + \omega_y^2 y^2 + \omega_z^2 z^2\right), \tag{1}$$

where m is the mass of a ^{87}Rb atom and ω_i are the trap frequencies. The blue-detuned Gaussian barrier propagates along z and is effectively uniform along y:

$$U_E(x, z) = \frac{U_0}{1 + (z/z_R)^2} \exp\left[-\frac{2x^2}{\omega_0^2 \left(1 + (z/z_R)^2\right)}\right], \tag{2}$$

where U_0 is the peak barrier height, ω_0 the waist at focus, and z_R the Rayleigh range.

If the beam waist minimum is displaced by an axial offset o from the trap center, the total potential becomes

$$U_T(x, y, z; o) = U_B(x, y, z) + \frac{U_0}{1 + \left((z + o)/z_R\right)^2} \times \exp\left[-\frac{2x^2}{\omega_0^2 \left(1 + ((z + o)/z_R)^2\right)}\right]. \tag{3}$$

B. Atomic Motion Dynamics

Atomic trajectories follow Newton's equations from Eq. (3):

$$\ddot{x} = \frac{4U_0 x}{m\omega_0^2 \left[1 + \left(\frac{z+o}{z_R}\right)^2\right]^2} \exp\left[-\frac{2x^2}{\omega_0^2 \left(1 + \left(\frac{z+o}{z_R}\right)^2\right)}\right] - \omega_x^2 x, \tag{4}$$

$$\ddot{y} = -\omega_y^2 y, \tag{5}$$

$$\ddot{z} = \frac{2U_0(z+o)}{mz_R^2\left[1+\left(\frac{z+o}{z_R}\right)^2\right]^2}\exp\left[-\frac{2x^2}{\omega_0^2\left(1+\left(\frac{z+o}{z_R}\right)^2\right)}\right] \times\left[1-\frac{2x^2}{\omega_0^2\left(1+\left(\frac{z+o}{z_R}\right)^2\right)}\right]-\omega_z^2 z. \tag{6}$$

Equations (4)–(6) are solved numerically for ensembles of atoms drawn from a canonical distribution at temperature T. While these trajectories provide exact positions, imaging systems observe a blurred optical-density (OD) distribution. We therefore convolve each atom with a Gaussian point-spread function

$$\mathrm{PSF}(x, y, z) = \exp\left[-\frac{x^2+y^2}{2\sigma_{PBS}{}^2(z)}\right], \tag{7}$$

where the imaging blur σ_{PBS} depends on the numerical aperture (NA) and the imaging wavelength λ [16]:

$$\sigma_{PBS}(z) = \frac{0.21\,\lambda}{\mathrm{NA}}\sqrt{1+\left(\frac{z}{z_R}\right)^2}. \tag{8}$$

Simulated OD images are analyzed using the same Gaussian fit model used in the experiment.

C. Collision and Rethermalization

Collisions are included using a classical two-body scattering model. The collision rate

$$f_{\mathrm{col}} = n\,\sigma_s\,\bar{v} \tag{9}$$

depends on the density n, the scattering cross-section σ_s, and the mean relative speed

$$\bar{v} = \sqrt{\frac{16k_B T}{\pi m}}. \tag{10}$$

Two atoms are considered to collide when their separation falls below a threshold set by σ_s. Elastic collisions are resolved by exchanging momentum along the interatomic axis:

$$\vec{v}_{1f} = \vec{v}_{1i} + \left[(\vec{v}_{1i} - \vec{v}_{2i})\cdot\hat{n}\right]\hat{n}, \tag{11}$$

$$\vec{v}_{2f} = \vec{v}_{2i} - \left[(\vec{v}_{1i} - \vec{v}_{2i})\cdot\hat{n}\right]\hat{n}, \tag{12}$$

where $\vec{v}_{1f}$ and $\vec{v}_{2f}$ are the initial final velocities of atoms 1 and 2, and $\hat{n}$ is randomized to emulate s-wave scattering.

D. Cloud Separation

We employ two separation measures in this work.

(1) Image-based separation (experimental metric). The column-integrated OD is fit to

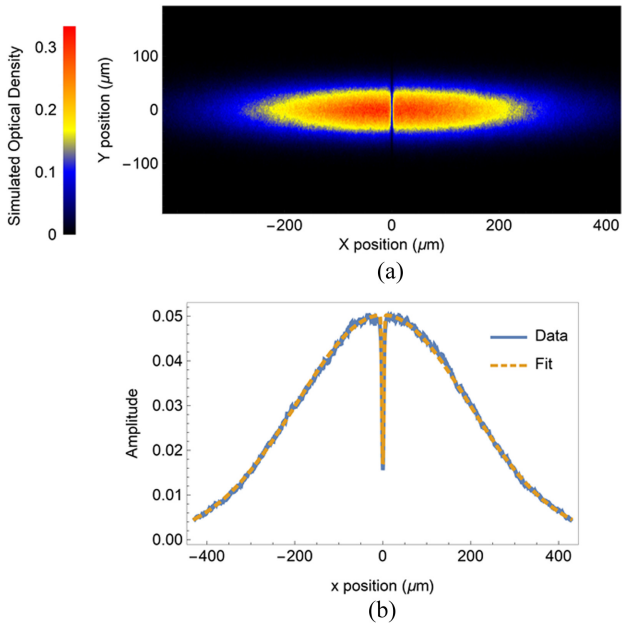

Fig. 2. (a) Example averaged OD image obtained from simulation. (b) Column-averaged OD profile and bimodal Gaussian fit used to extract the cloud separation.

$$f(x) = A_1 e^{-x^2/2\sigma_1^2} - A_2 e^{-x^2/2\sigma_2^2} + C, \tag{13}$$

where A_1, A_2, σ_1, σ_2, and C are positive constants, and σ_2 defines the measured separation. Figure 2(b) shows an example of this fit applied to the column sum of the OD image in Fig. 2(a).

(2) Energy-threshold separation (theoretical metric). Atoms with energy below the effective barrier height

$$E_c(z; o) = \frac{U_0}{1+\left(\frac{z+o}{z_R}\right)^2} \tag{14}$$

remain confined and form two clouds. We define the average energy of the sub-barrier population as

$$\langle E\rangle_{E<E_c} = \frac{\int_0^{E_c} E\, f_E(E)\,\mathrm{d}E}{\int_0^{E_c} f_E(E)\,\mathrm{d}E}, \tag{15}$$

where the Maxwell–Boltzmann kinetic-energy distribution is

$$f_E(E) = 2\sqrt{\frac{E}{\pi}}\left(\frac{1}{k_B T}\right)^{3/2} e^{-E/k_B T}. \tag{16}$$

The corresponding axial positions on the Gaussian barrier determine the theoretical cloud separation. Because the two definitions reflect distinct physical processes—image blur versus ensemble energetics—their absolute values need not coincide, but their extrema and trends do.

Two qualitative consequences of the combined potential are worth noting. First, any nonzero offset pushes atoms preferentially toward the opposite side of the barrier: for a negative offset, atoms experience a lower effective barrier at some higher z than the offset and beyond. Second, if the axial trap frequency ω_z is

too low, the derivative of the total potential with respect to z can become negative near the trap center. In this case, it is energetically easier for atoms to move along z and traverse the barrier at a location, where it is effectively lower than at $z = 0$. This behavior allows atoms to travel "around" the barrier rather than through it and can complicate the interpretation of tunneling and transport dynamics.

3. SIMULATION

To validate the alignment criteria introduced in this work, we perform large-scale numerical simulations of atom dynamics in the full potential U_T defined previously. The simulation incorporates realistic initial conditions, numerical integration of the equations of motion, and elastic two-body collisions, followed by image-level analysis using the same separation metrics applied in the experiment.

The simulation begins by defining all physical parameters (mass, temperature, trap frequencies, and beam properties) as well as numerical parameters such as the integration time step. Initial positions and velocities for all atoms are then drawn from the appropriate thermal distributions.

Each atom's trajectory is computed using a numerical ordinary differential equation (ODE) solver. The longitudinal and transverse dynamics in the $x-z$ plane are obtained by integrating Eqs. (4)–(6), whereas the y axis motion, governed by a simple harmonic oscillator, is calculated analytically from its amplitude and phase. After every integration step, atoms are checked for possible collisions. When two atoms approach within the specified scattering radius, their velocities are updated according to Eqs. (11) and (12). Positions are not modified during collision events, and the updated states are passed to the next integration cycle. The simulation proceeds with a fixed time step until the total evolution time is reached.

Accurate collision handling places constraints on the choice of time step. The step size must be small enough to prevent unphysical three-body encounters and to capture grazing collisions that might otherwise be missed. Although an infinitesimally small step would guarantee perfect collision resolution, this is computationally impractical. We also note that a truncated Maxwell–Boltzmann distribution rethermalizes within approximately five collision times [17]; for a 25 μK ensemble, this corresponds to roughly 15 ms. Empirically, we find that choosing a step size such that atoms move, on average, no more than 2% of the scattering radius per step is sufficient to capture nearly all collisions while maintaining numerical stability. This criterion is adopted throughout this work.

Computational considerations further constrain the simulation design. A physically realistic sample of 5×10^5 atoms would require several days of computation. To reduce the cost, we use the scaling implied by Eq. (9): decreasing the number of simulated atoms while proportionally increasing the collision cross section preserves the overall collision rate. In practice, we simulate 20,000 atoms with an appropriately scaled cross section, achieving good physical fidelity with manageable computation times.

A. Position and Velocity Sampling

Velocities are sampled from the Maxwell–Boltzmann distribution. Each component is drawn from a normal distribution with variance

$$\sigma_v = \sqrt{\frac{k_B T}{m}}, \tag{17}$$

and for a purely harmonic potential the corresponding spatial distribution is also Gaussian with variances

$$\sigma_i = \sqrt{\frac{k_B T}{m\omega_i^2}}, \tag{18}$$

where $i \in \{x, y, z\}$. Because the y dynamics remain exactly harmonic throughout the simulation, y is sampled directly from Eq. (18), and the initial (y, v_y) pair uniquely determines the subsequent sinusoidal motion along that axis.

In contrast, the combined magnetic plus Gaussian optical potential is not harmonic along x or z, so direct Gaussian sampling is not appropriate. Instead, we use rejection sampling [18]. Trial positions are drawn uniformly from the ranges

$$-6\sigma_x \le x \le 6\sigma_x, \qquad z_{\min} - 6\sigma_z \le z \le z_{\min} + 6\sigma_z,$$

where $z_{\min}$ is the minimum of U_T. The probability associated with each trial position is normalized by the maximum probability at the global minimum; the position is accepted if the ratio exceeds a uniformly distributed random number in [0, 1]. This procedure yields correct sampling from the canonical spatial distribution in the full potential.

B. Monte Carlo Sampling

The theoretical separation curves presented earlier do not reveal whether a separation is experimentally *detectable*. Because the theoretical model is continuous, a nonzero fraction of atoms below the barrier always exists in principle. However, in a finite ensemble at high temperatures, the number of sub-barrier atoms may become too small to produce a visible double-peak structure in the OD image.

To estimate detectability, we perform Monte Carlo sampling [19,20]. For each temperature, we draw a large number of random atoms (typically 5×10^5) from the canonical distribution and compute the average sub-barrier energy $\langle E \rangle_{E<E_c}$. If no statistically significant population satisfies $E < E_c$, then a measurable separation is unlikely to appear in simulated or experimental images. This approach identifies regions in parameter space (temperature, trap frequency, and beam offset), where the double-well structure is experimentally resolvable.

4. RESULTS

The cloud temperature and the axial trap frequency ω_z are the parameters that most strongly influence the observed separation, as they govern the fraction of atoms confined near the Gaussian barrier. Unless otherwise stated, simulations use 20,000 atoms, an e^{-2} beam waist of 1.1 μm, a peak barrier height of 10 MHz, a Rayleigh range $z_R = 4.94$ μm, and transverse trap frequencies $\omega_x = 2\pi \times 40$ Hz and

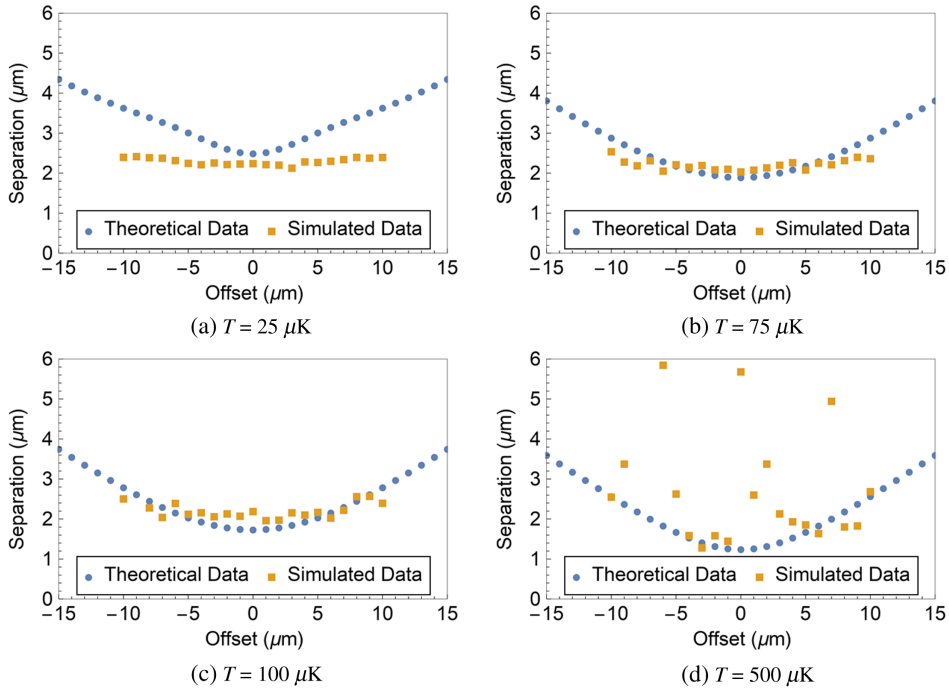

(a) $T = 25\ \mu K$ (b) $T = 75\ \mu K$

(c) $T = 100\ \mu K$ (d) $T = 500\ \mu K$

Fig. 3. Simulated cloud separation (squares) and theoretical energy-based separation (points) as a function of axial beam offset for temperatures of 25, 75, 100, and 500 μK. Colder clouds yield a well-defined minimum separation and closely track the theoretical trend. At high temperature ($\gtrsim$500 μK), thermal broadening and finite sampling cause irregular or noisy separations.

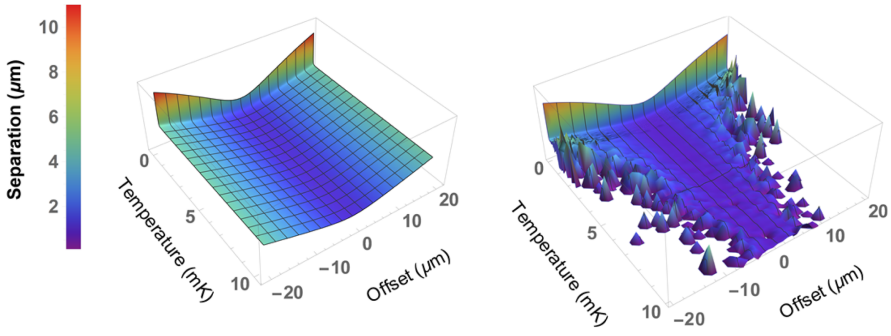

(a) Theory (b) Monte Carlo sampling

Fig. 4. Temperature-dependent separation curves obtained from (a) analytical energy-based theory and (b) Monte Carlo sampling over temperatures from 1 μK to 10 mK. Both approaches indicate that the minimum separation occurs at zero offset for all temperatures, although detectability deteriorates at high T due to the diminished sub-barrier population.

$\omega_y = 2\pi \times 484$ Hz, consistent with standard atom-chip configurations [6].

Figure 3 shows the simulated and theoretical separations for the four temperatures. At $T = 25-100$ μK, the simulated minima align well with theoretical predictions, confirming that the lowest measurable separation corresponds to optimal alignment. At $T = 500$ μK, the separation becomes irregular due to undersampling of the sub-barrier population: even ensembles with 5×10^5 atoms fail to capture the small low-energy tail responsible for confinement.

Figure 4 extends the temperature sweep from 1 μK to 10 mK, comparing the theoretical separation to Monte Carlo estimates. Both methods confirm that the separation minimum always occurs at zero offset, but the Monte Carlo results make clear that above a few hundred μK the finite ensemble may fail to produce a visible separation even when one exists theoretically.

The axial-trap-frequency dependence is summarized in Fig. 5, showing that tighter axial confinement produces a clearer and more robust minimum in the separation curve. The discrepancy between the theoretical and simulation separation in Fig. 5(d) comes from the simple fact that the definitions for the separations are different and become more pronounced when the atoms are tightly confined in the z axis.

Theoretical sweeps of ω_z and beam waist ω_0 in Fig. 6 confirm that while these parameters shift the magnitude of the separation, the location of the minimum remains fixed at zero offset. Increasing ω_z compresses the cloud axially, improving detectability; increasing ω_0 widens the barrier and increases the absolute separation, but the minimum remains unchanged.

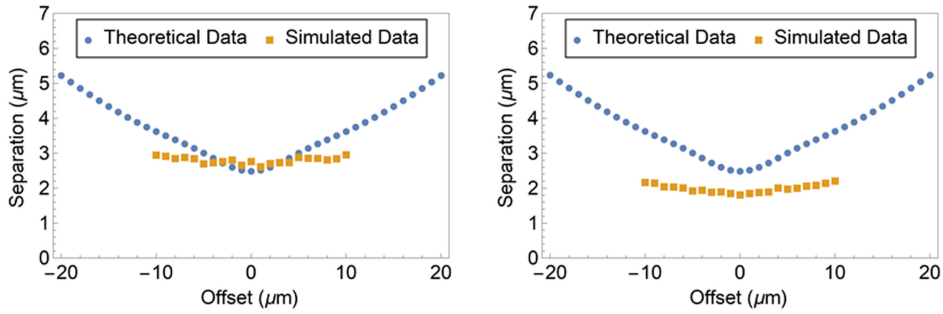

(a) $\omega_z/2\pi$ = 300 Hz (b) $\omega_z/2\pi$ = 700 Hz

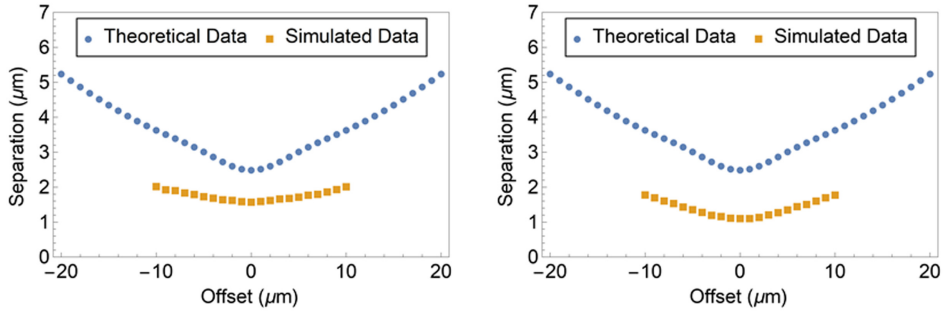

(c) $\omega_z/2\pi$ = 1 kHz (d) $\omega_z/2\pi$ = 10 kHz

Fig. 5. Simulated cloud separation (squares) and theoretical energy-based separation (points) as a function of axial beam offset for z axis trap frequencies of 300, 700, 1000, and 10,000 Hz. Increasing ω_z confines atoms more strongly along z, improving the clarity and sharpness of the separation minimum.

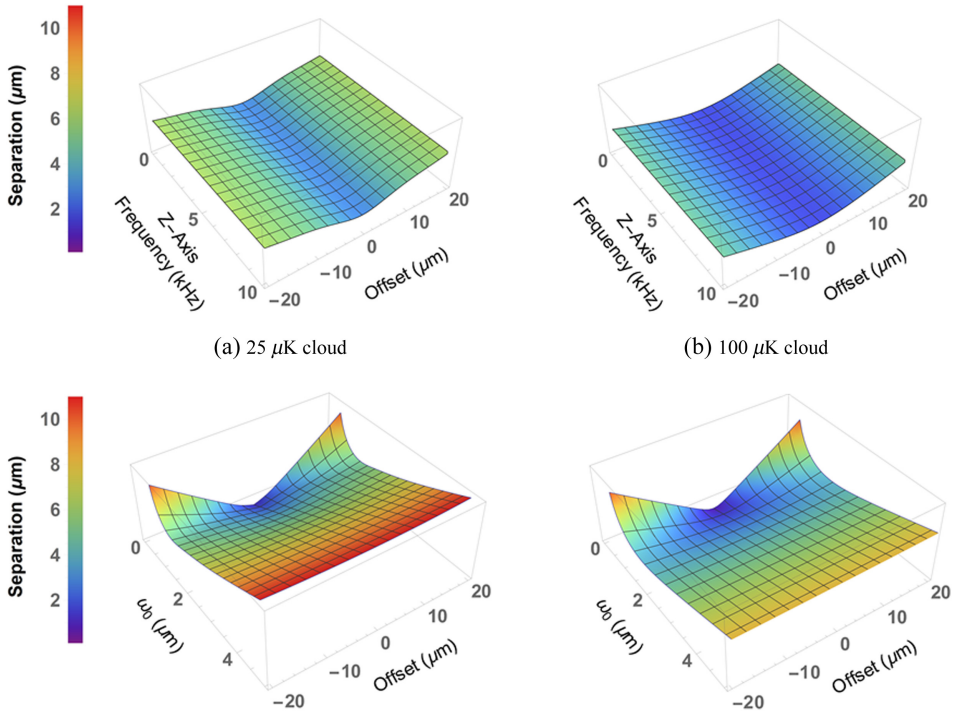

(a) 25 μK cloud (b) 100 μK cloud

(c) Beam waist sweep at 25 μK (d) Beam waist sweep at 100 μK

Fig. 6. Theoretical separation curves for (top row) varying axial trap frequency ω_z and (bottom row) varying Gaussian beam waist ω_0. In all cases, the global minimum occurs at zero offset, confirming that perfect alignment always minimizes the separation, even when the absolute scale of the separation varies.

Across all temperatures, trap frequencies, and beam parameters explored here, both simulation and theory consistently show that (i) the cloud separation is minimized when the optical barrier is centered on the magnetic trap; (ii) lower temperatures and higher axial confinement produce cleaner, more experimentally resolvable minima; and (iii) deviations between simulated

and theoretical curves arise from their differing definitions and from finite-size sampling, not from discrepancies in physical behavior. These results provide clear operational guidance for experiments: optimal alignment is reliably obtained by minimizing the measured cloud separation, and this criterion becomes increasingly robust at low temperature and high axial trap frequency. Of course, there might be other sources of noise or uncertainty that might impact the feasibility of the detecting separations on the order of 1–2 μm, such as thermal flexing in the atom chip, but the value presented here is that the separation-based method for judging the focus remains useful under various temperatures, z axis trap frequency, and simulated imaging.

5. CONCLUSION

We have developed and validated an image-aware simulation framework for analyzing atom-cloud separation in a three-dimensional harmonic trap bisected by a blue-detuned Gaussian optical barrier. The framework integrates (i) a first-principles dynamical model based on the coupled equations of motion [Eqs. (4)–(6)], together with a realistic imaging pipeline using PSF-based optical-depth rendering, and (ii) an energy-threshold model derived from a truncated Maxwell–Boltzmann distribution. Complementary Monte Carlo sampling was employed to identify the parameter regimes, where a separation is experimentally detectable in finite atomic ensembles. Across all methods, a consistent conclusion emerges: the optimal alignment of the optical barrier corresponds to the minimum measurable separation between the two atom clouds.

Systematic parameter scans reinforce this result. At low temperatures (e.g., $T = 25$ μK), simulated separations closely follow theoretical predictions (Fig. 3), whereas increasing temperature broadens the energy distribution and reduces the size of the sub-barrier population, degrading detectability (Figs. 3 and 4). In the high-temperature regime ($\gtrsim$500 μK), finite-sampling effects dominate: even very large ensembles (5×10^5 sampled atoms) undersample the low-energy tail, producing irregular or "chaotic" apparent separations. In contrast, increasing the axial confinement strengthens localization near the barrier and sharpens the separation minimum (Fig. 5). Although the simulated and theoretical curves differ in definition and therefore need not coincide quantitatively, their extrema and qualitative behaviors align, supporting the minimum-separation rule as a reliable alignment criterion. Additionally, other experimental noise, such as thermal flexing on an atom chip, may prevent direct measurements of separations on the order of 1–2 μm. Other, perhaps complementary measurement techniques such as matter-wave interferometry during time-of-flight imaging could potentially allow for higher precision at such separation distances.

The analysis also highlights several practical considerations. First, detectability is fundamentally a finite-number problem: a separation may exist theoretically while remaining invisible experimentally if too few atoms occupy the sub-barrier region. Monte Carlo sampling from 1 μK to 10 mK identifies these boundaries. Second, tractable simulations can be maintained by scaling the collision cross section when reducing atom number, ensuring that the collision rate $f_{\mathrm{col}} = n\sigma_s \bar{v}$ is preserved, and by choosing time steps small enough to resolve two-body collisions (empirically, steps corresponding to ∼2% of the collision radius are sufficient). Third, the model reveals parameter-dependent transport pathways: insufficient axial confinement can allow atoms to move along z and traverse the barrier, where it is effectively lower, potentially confounding tunneling or transport measurements if not accounted for during alignment scans.

Several simplifying assumptions define the scope of this study. The magnetic potential is modeled as harmonic, the optical barrier as a Gaussian sheet with infinite extent along y, and imaging blur via a Gaussian PSF. Collisions are treated as classical elastic events with randomized scattering directions to emulate s-wave behavior, and rethermalization is governed by two-body processes controlled by the time-step choice. The offset is restricted to the axial direction, and optical aberrations and beam astigmatism are neglected. These approximations make the calculations tractable while retaining the essential physics underlying separation formation and detectability.

In summary, despite realistic imaging effects, collisional dynamics, and finite sampling, our combined theoretical, numerical, and Monte Carlo analysis shows that the minimum measured separation offers a robust and experimentally practical metric for aligning a Gaussian optical barrier to the center of a magnetic trap. The results provide clear guidance for cold-atom experiments: operate at as low a temperature and as high an axial trap frequency as feasible, and use the experimentally observed separation minimum as a reliable indicator of optimal alignment.

Funding. U.S. National Science Foundation (2228725).

Disclosures. The authors declare that there are no conflicts of interest related to this paper.

Data availability. Data underlying the results presented in this paper are not publicly available at this time but may be obtained from the authors upon reasonable request.

REFERENCES

1. K. O. Chong, J.-R. Kim, J. Kim, *et al.*, "Observation of a non-equilibrium steady state of cold atoms in a moving optical lattice," Commun. Phys. **1**, 25 (2018).
2. S. V. Prants, "Chaotic dynamics of cold atoms in multidimensional optical lattices," J. Russ. Laser Res. **45**, 395–403 (2024).
3. C. Xue, S. Dai, and B. Cui, "Transport properties of cold atoms in optical lattice," Laser Phys. **31**, 105501 (2021).
4. H. P. Mishra, A. S. Flores, W. Vassen, *et al.*, "Efficient production of an ^{87}Rb F = 2, $m_F = 2$ Bose-Einstein condensate in a hybrid trap," Eur. Phys. J. D At. Mol. Opt. Phys. **69**, 52 (2015).
5. P. J. Bardroff, I. Bialynicki-Birula, D. S. Krähmer, *et al.*, "Dynamical localization: classical vs quantum oscillations in momentum spread of cold atoms," Phys. Rev. Lett. **74**, 3959–3962 (1995).
6. S. C. Caliga, C. J. E. Straatsma, and D. Z. Anderson, "Transport dynamics of ultracold atoms in a triple-well transistor-like potential," New J. Phys. **18**, 025010 (2016).
7. R. Christie and J. Eastman, "Quantum tunnelling and thermally driven transitions in a double-well potential at finite temperature," J. Phys. A Math. Theor. **57**, 235005 (2024).
8. V. I. Yukalov and E. P. Yukalova, "Cold atoms in double-well optical lattices," Phys. Rev. A At. Mol. Opt. Phys. **78**, 063610 (2008).
9. A. E. Afanasiev, P. I. Skakunenko, D. V. Bykova, *et al.*, "Atom chip," Phys. Usp. **67**, 1084–1094 (2024).
10. R. Folman, P. Krüger, J. Schmiedmayer, *et al.*, "Microscopic atom optics: from wires to an atom chip," Adv. At. Mol. Opt. Phys. **48**, 263–356 (2002).

11. S. Nandi, "The quantum gaussian well," Am. J. Phys. **78**, 1341–1345 (2010).
12. S. Campbell, G. De Chiara, and M. Paternostro, "Equilibration and nonclassicality of a double-well potential," Sci. Rep. **6**, 19730 (2016).
13. I. Stroescu, D. B. Hume, and M. K. Oberthaler, "Dissipative double-well potential for cold atoms: Kramers rate and stochastic resonance," Phys. Rev. Lett. **117**, 243005 (2016).
14. T. Schumm, S. Hofferberth, L. M. Andersson, *et al.*, "Matter-wave interferometry in a double well on an atom chip," Nat. Phys. **1**, 57–62 (2005).
15. J. M. Zhang, W. M. Liu, and D. L. Zhou, "Cavity QED with cold atoms trapped in a double-well potential," Phys. Rev. A At. Mol. Opt. Phys. **77**, 033620 (2008).
16. H. Ma, R. Fu, J. Xu, *et al.*, "A simple and cost-effective setup for super-resolution localization microscopy," Sci. Rep. **7**, 1542–1549 (2017).
17. D. W. Snoke and J. P. Wolfe, "Population dynamics of a Bose gas near saturation," Phys. Rev. B Condens. Matter **39**, 4030–4037 (1989).
18. G. Biondini, "An introduction to rare event simulation and importance sampling," in *Handbook of Statistics* (Elsevier Science & Technology, 2015), Vol. **33**, pp. 49–52.
19. R. K. Pathria and P. D. Beale, *Statistical Mechanics* (Academic Press, 2011).
20. R. S. Dumont, "Monte Carlo sampling for atomic and molecular clusters with fixed energy and angular momentum," J. Chem. Phys. **96**, 2203–2216 (1992).